Journal of Advanced Ceramics
2022, **11**(1): 105–119
https://doi.org/10.1007/s40145-021-0520-z
ISSN 2226-4108
CN 10-1154/TQ

Research Article

Carbonized wood with ordered channels decorated by $NiCo_2O_4$ for lightweight and high-performance microwave absorber

Guangyu QIN[a], Xiaoxiao HUANG[a,*], Xu YAN[b], Yunfei HE[a], Yuhao LIU[a], Long XIA[c,*], Bo ZHONG[c]

[a]*School of Materials Science and Engineering, Harbin Institute of Technology, Harbin 150001, China*
[b]*Beijing Institute of Radio Measurement, Beijing 100854, China*
[c]*School of Materials Science and Engineering, Harbin Institute of Technology at Weihai, Weihai 264009, China*

Received: April 27, 2021; Revised: June 13, 2021; Accepted: July 8, 2021

Abstract: Wood-derived carbon has a 3D porous framework composed of through channels along the growth direction, which is a suitable matrix for preparing electromagnetic wave (EMW) absorbing materials with low cost, light weight, and environmental friendliness. Herein, the carbonized wood decorated by short cone-like $NiCo_2O_4$ ($NiCo_2O_4$@CW) with highly ordered straight-channel architecture was successfully manufactured through a facile calcination procedure. The horizontal arrangement of the through channels of $NiCo_2O_4$@CW (H-$NiCo_2O_4$@CW) exhibits a strong reflection loss value of −64.0 dB at 10.72 GHz with a thickness of 3.62 mm and a low filling ratio of 26 wt% (with the density of 0.98 g·cm^{-3}), and the effective absorption bandwidth (EAB) is 8.08 GHz (9.92–18.0 GHz) at the thickness of 3.2 mm. The excellent microwave absorption (MA) property was ascribed to the ordered-channel structure with abundant interfaces and defects from $NiCo_2O_4$@CW, which could promote the interfacial polarization and dipole polarization. What is more, this advantageous structure increased the multiple reflections and scattering. Finite element analysis (FEA) simulation is carried out to detect the interaction between the prepared material and EMW when the ordered channels are arranged in different directions. This research provides a low-cost, sustainable, and environmentally friendly strategy for using carbonized wood to fabricate microwave absorbers with strong attenuation capabilities and light weight.

Keywords: microwave absorption (MA); wood-derived carbon; ordered-channel architecture; light weight; finite element analysis (FEA)

1 Introduction

Due to the serious problem of electromagnetic pollution and the urgent need of military anti-reconnaissance capabilities, a variety of electromagnetic wave (EMW) absorbing materials with excellent performance have been developed, which attenuate EMW by converting them into other forms of energy [1,2]. Among various microwave absorbing materials, the carbonaceous materials have been paid high attention due to their chemical stability, low density, and tunable electromagnetic parameters. In past reports, commonly used carbon materials for microwave absorption (MA), such

* Corresponding authors.
E-mail: X. Huang, swliza@hit.edu.cn;
L. Xia, xialonghit@gmail.com

as carbon fiber [3], carbon nanotube (CNT) [4–6], metal-organic framework (MOF) [7], and graphene [8], exhibited good MA performance. Carbon materials have greatly promoted the development of absorbing materials.

Simultaneously, the concept of sustainable development and environmental friendliness is also being valued more and more. Traditional carbon materials often rely on modern industrial techniques, which are complex and costly, and the by-products of the preparation process can damage the natural environment. Fortunately, the biomass-derived carbon overcomes the shortcomings of man-made carbon materials with many characteristics such as light weight, large natural reserves, and low cost. Nowadays, the natural wood-derived carbon materials with through channels parallel to the growth direction have been successfully applied in many fields, for example, energy storage materials, catalysts, and sensors [9–11]. The three-dimensional (3D) skeleton composed of orderly-arrangement and through channels existing in wood-derived carbon can also be applied to MA materials, which not only is favor of microwave scattering and multi-reflections to prolong the propagation path of EMW [12] and forms an efficient conductive network to enhance the conductive loss [13], but also provides a load position for magnetic materials to improve impedance matching and cause magnetic loss [14]. Hence, this 3D porous structure can be used as an ideal carbon substrate for electromagnetic interference (EMI) shielding and MA materials.

Xi *et al.* [15] reported that wood-based straight channel structure, which was analogous to a waveguide, exhibited excellent MA performance with maximum reflection loss (RL) of −68.3 dB at 4.28 mm and effective absorption bandwidth (EAB) (RL < −10 dB) up to 7.63 GHz at 3.73 mm. This unique structure has provided inspiration for the subsequent design of wood-derived carbon MA materials. Zheng *et al*. [13] have successfully fabricated the wood-derived magnetic porous carbon composites with a highly ordered anisotropic porous architecture on the foundation of the 3D ordered-channel skeleton, and this Ni/porous carbon composite exhibited an exceptional EMI shielding effectiveness of 50.8 dB at the whole X band (8.2–12.4 GHz) with the thickness of 2 mm.

In order to make full use of the 3D ordered porous framework derived from wood-derived carbon, our research introduces $NiCo_2O_4$ mixture on the wall of highly ordered straight channels inherited from wood. The $NiCo_2O_4$, a spinel-structure bimetal oxide, with high electrochemical activity, was mainly used in the electrochemistry field [16,17]. Therefore, from the point of its high electronic conductivity, $NiCo_2O_4$ has great potential value in the field of absorber with superior dielectric loss [14,18]. It can be foreseen that various loss mechanisms make as-prepared samples obtain excellent absorbing performance due to the natural favorable structure, improved impedance matching, and optimized conductivity. Furthermore, the finite element simulation of $NiCo_2O_4$@CW testifies that horizontal arrangement of the through channels leads to the excellent EMW attenuation ability. Our study provides an alternative strategy to using low-priced, environmentally friendly natural wood, and simple, efficient preparation procedure to design microwave absorbers with high absorption efficiency and wide absorption frequency. We hope that this work lays a significant foundation for the design and application of wood-derived carbon absorbers to fulfill the ever-growing demands.

2 Experimental

2.1 Preparation of CW

All reagents used in our experiments were used as received without further purification. Poplar wood was purchased from plantation (Hubei, China). To prepare the lignin removal solution, 4 g $NaClO_2$ (80%; Shanghai Macklin Biochemical Co., Ltd., China) and 1.35 mL CH_3COOH (99.5% AR; Tianjin Fuyu Fine Chemical Co., Ltd., China) were dissolved in 400 mL deionized water. Then a slice of poplar wood slice cut into 10 mm × 10 mm × 10 mm was immersed in the as-prepared solution in the beaker at 80 ℃ for 12 h. The lignin-removed wood (LFW) was prepared. Finally, the LFW was placed in a tubular furnace and carbonized at 400 ℃ under flowing nitrogen for 1.5 h with a heating rate of 3 ℃·min^{-1}. The CW was placed in a vacuum drying oven for further use.

2.2 Synthesis of $NiCo_2O_4$@CW composites

The CW was immersed in the solution of 1 mol·L^{-1} of $Ni(NO_3)_2·6H_2O$ and 2 mol·L^{-1} of $Co(NO_3)_2·6H_2O$ (98% AR; Tianjin Fengchuan Chemical Reagent Technologies Co., Ltd., China) in the beaker. The

beaker was placed in ultrasonic environment for 30 min, then allowed to stand for 12 h with −0.1 MPa environment, and finally heated at 50 ℃ for 6 h. The CW was fully saturated with $Ni(NO_3)_2{\cdot}6H_2O$ and $Co(NO_3)_2{\cdot}6H_2O$ solution. Subsequently, the CW/$Ni(NO_3)_2{\cdot}6H_2O$/$Co(NO_3)_2{\cdot}6H_2O$ composite was placed in a drying oven for 12 h with 60 ℃. Finally, the as-obtained material was placed in a tubular furnace for heating to 300 ℃ for 1 h in air. After the temperature dropped to room temperature, the $NiCo_2O_4$@CW hybrid was obtained. For comparison, the CW was also post treated by the same calcination conditions, and the post-treated CW was prepared.

2. 3 Characterization

Powder XRD pattern was recorded on BRUKER diffractometer using Cu Kα radiation. The morphology and microstructure were observed using SEM images on SUPRA™55 (ZEISS, UK) at high current of 20 kV. The elemental composition was detected by energy dispersive spectrometer (EDS) spectrum deriving from the SEM, coupled with copper grids. Raman spectra were obtained by a Renishaw Raman microscope using an Ar ion laser (532 nm). Thermogravimetric analysis (TGA) measurements for the composite were carried out by a DTG-60H thermal analyzer (Japan) under flowing oxygen atmosphere and with a heating rate of 10 ℃·min^{-1}. The X-ray photoelectron spectroscopy (XPS) measurements were recorded on KRATOS Axis $Ultra^{DLD}$ (UK) equipped with a monochromatic X-ray source (Al Kα, $h\nu$ = 1486.6 eV). The room temperature hysteresis loop was performed on vibrating sample magnetometer (VSM; JDAW-2000C&D, Changchun Yingpu Co., Ltd., China). The conductivity measurements of all samples were carried out by the 2450 Source Meter (KEITHIEY Co., Ltd, USA).

2. 4 Electromagnetic parameter measurements

The electromagnetic (EM) parameters were obtained on vector network analyzer (Agilent, N5230A, USA) by the T/R coaxial line method at 2–18 GHz band. Testing samples of MA were prepared by cutting method, which can retain the micron-level structure inside the material. Two pieces of $NiCo_2O_4$@CW materials were tailored into cylindrical toroidal specimens along parallel to the wood growth direction and perpendicular to the wood growth direction (called vertical and horizontal) with an outer diameter of 7.00 mm and inner diameter of 3.00 mm, and then were immersed in liquid paraffin wax; after solidification, the sample was prepared, named V-$NiCo_2O_4$@CW and H-$NiCo_2O_4$@CW. In the same way, the CW material was cut into cylindrical toroidal specimens, named V-CW (vertical) and H-CW (horizontal). The average filling ratio of coaxial sample was 26 wt% (with the density of 0.98 g·cm^{-3}) and 21 wt%, obtained by weighing several times. In addition, the disordered samples (named CW and $NiCo_2O_4$@CW) were prepared by mixing the powders with paraffin matrix and pressed into a toroidal ring with an outer diameter of 7.00 mm and inner diameter of 3.00 mm, respectively, with the same filling ratio of ordered-channel samples. The RL values were obtained by EM parameters on the basis of transmission line theory, which can be calculated by the following equations based on the metal back-panel model [19,20]:

$$Z_{\text{in}} = Z_0\sqrt{\frac{\mu_{\text{r}}}{\varepsilon_{\text{r}}}}\tanh\left(\text{j}2\pi\frac{fd\sqrt{\mu_{\text{r}}\varepsilon_{\text{r}}}}{c}\right) \quad (1)$$

$$\text{RL(dB)} = 20\lg\left|\frac{Z_{\text{in}} - Z_0}{Z_{\text{in}} + Z_0}\right| \quad (2)$$

where Z_{in} is the input impedance of absorber, Z_0 is the impedance of free space, ε_{r} and μ_{r} represent the complex permittivity ($\varepsilon_{\text{r}} = \varepsilon' - \text{j}\varepsilon''$) and the complex permeability ($\mu_{\text{r}} = \mu' - \text{j}\mu''$), respectively, f indicates the frequency of the incident microwaves, d means the thickness of the microwave absorber, and c is the velocity of the microwave. RL is smaller than −10 dB, which is implied that more than 90% of the microwave is absorbed by MA, and the frequency range can be considered as EAB [21].

3 Results and discussion

The preparation procedure of $NiCo_2O_4$@CW with the structure of oriented channels and standard coaxial samples is schematically illustrated in Fig. 1.

The crystallographic structures of CW and $NiCo_2O_4$@CW were characterized by powder XRD, as shown in Fig. 2(a). The broad diffraction peaks at 26.23° and 44.35° correspond to the (200) and (101) crystal planes of graphite crystal structure, respectively, indicating that CW is partially graphitized at 400 ℃, behaving as amorphous carbon. For the $NiCo_2O_4$@CW

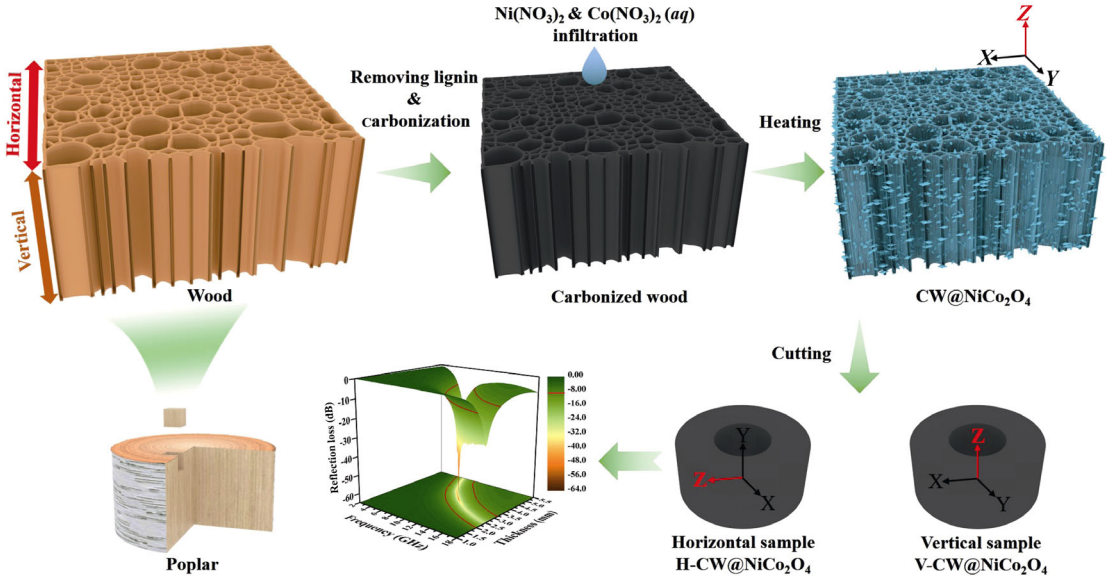

Fig. 1 Fabrication process of $NiCo_2O_4$@CW with ordered channels, and schematic illustration to obtain vertical and horizontal standard coaxial samples.

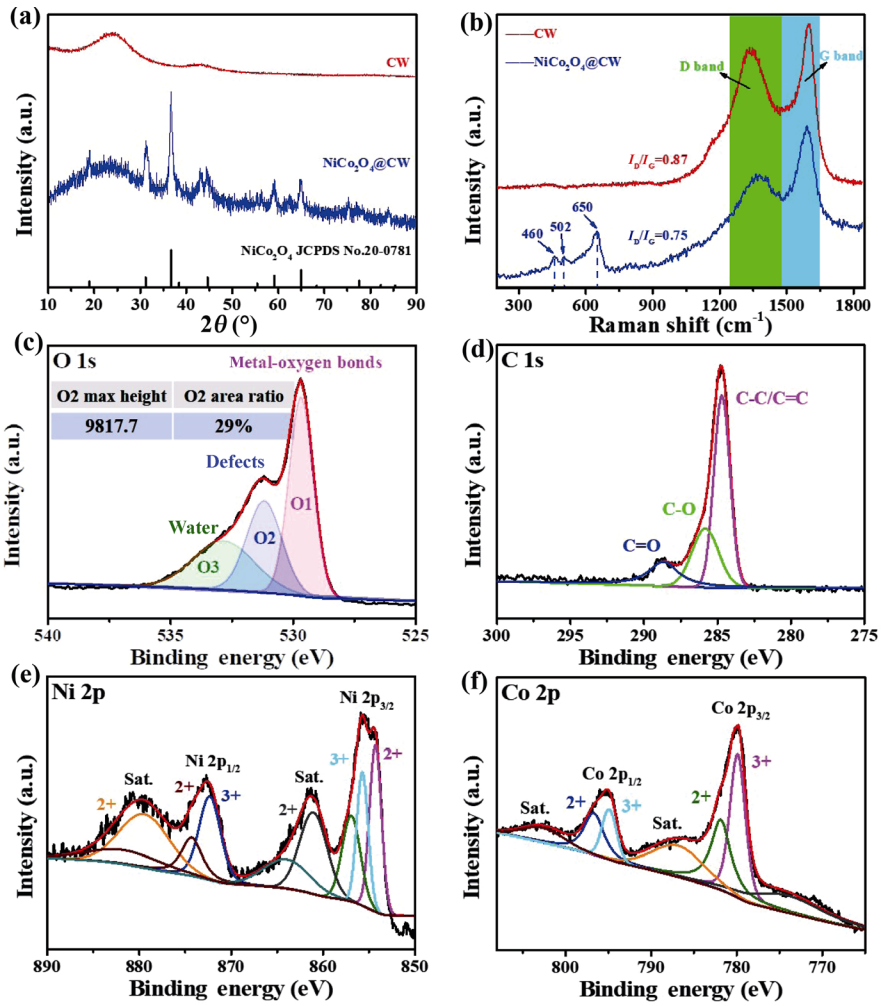

Fig. 2 (a) XRD patterns of CW and $NiCo_2O_4$@CW and (b) Raman spectra of CW and $NiCo_2O_4$@CW; XPS spectra of $NiCo_2O_4$@CW: (c) O 1s, (d) C 1s, (e) Ni 2p, and (f) Co 2p.

powder sample, the diffraction peak positions were consistent with the standard XRD pattern of $NiCo_2O_4$ (JCPDS No. 20-0781). The diffraction peaks of $NiCo_2O_4$@CW composites located at 31.3°, 36.8°, 44.3°, 59.1°, and 65.1° could be corresponded to the (220), (311), (400), (511), and (440) crystal planes of $NiCo_2O_4$ phase, respectively. Simultaneously, the broad diffraction peaks of amorphous carbon were obtained in the spectrum of $NiCo_2O_4$@CW composites. These results confirmed that $NiCo_2O_4$ was successfully deposited in through channel of CW. The mass fraction of carbon in $NiCo_2O_4$@CW composites is obtained by TGA, described in Fig. S1 in the Electronic Supplementary Material (ESM), which indicated the weight ratio of CW is 56.2 wt%.

Raman spectrum was applied to demonstrate the chemical environment of carbon atoms in the CW and $NiCo_2O_4$@CW powder, which is an important factor for electron transportation and makes a significant impact on the electromagnetic parameters [22]. In addition, Raman spectrum was also used to characterize the existence of cobalt and nickel atoms. Two obvious peaks located at 1320 cm^{-1} (D band) and 1580 cm^{-1} (G band) can be demonstrated in Fig. 2(b). The intensity of the D band peak represents the number of defects or the degree of disorder in the sp^2-hybridized carbon atoms or amorphous carbon deposits, while the G band peak is associated with the in-plane vibrations of sp^2 atoms in a 2D hexagonal graphitic lattice. The degree of disorder of carbon in the material can be characterized by the ratio of D band to G band (I_D/I_G) [23]. As shown in Fig. 2(b), the intensity ratio value of I_D/I_G was 0.87 for CW, and this result is in good agreement with the amorphous carbon in XRD pattern. The I_D/I_G value of $NiCo_2O_4$@CW was 0.78, which suggested abundant defects exist in both CW and $NiCo_2O_4$@CW, and the existence of $NiCo_2O_4$ reduced the degree of disorder of carbon in the material, increasing the graphitization degree. The Raman spectrum of spinel Co_3O_4 has a high-frequency peak at 693 cm^{-1}, determined by the octahedral/Co^{3+} [24]. For $NiCo_2O_4$, as Co^{3+} (or Ni^{3+}) was replaced by Ni^{2+} (or Co^{2+}), the octahedral/Co^{3+} (or Ni^{3+}) peak weakens and shifts to lower frequency (Fig. 2(b), the band at 650 cm^{-1} of $NiCo_2O_4$@CW is assigned to the A_{1g} phonon excitations); simultaneously, the octahedral/Ni^{2+} peak was observed at 502 cm^{-1} resulted from Ni^{2+} substitution at octahedral sites. The peak at 460 cm^{-1} was caused by tetrahedral/Co^{2+} (or Ni^{2+}, assigned to the E_g phonon excitations). This result confirms the successful synthesis of spinel structured $NiCo_2O_4$. It can be inferred that the Ni^{2+} substitution at octahedral sites would induce the formation of dipole and dipole polarization [24,25], which is a benefit for EM wave attenuation and thus results in enhanced MA properties.

The chemical composition and the elemental valence state of the $NiCo_2O_4$@CW composites were further characterized by XPS. The wide span spectrum of $NiCo_2O_4$@CW composites indicated four typical peaks, corresponding to Ni 2p, Co 2p, O 1s, and C 1s (Fig. S2 in the ESM). The Ni 2p spectrum has two spin-orbit doublets of Ni^{2+} and Ni^{3+}, the binding energies at 854.2, 861.2, 874.4, and 879.6 eV belonged to Ni^{2+}, and the peaks at 872.4 and 855.8 eV were assigned to Ni^{3+}. The binding energies at around 861.3 and 879.9 eV were marked to the two shake-up satellite peaks (named as ‘‘Sat.’’) of nickel (Fig. 2(e)). Similarly, the Co 2p spectrum given in Fig. 2(f) consists of one spin-orbit doublet characteristic of Co^{2+} (binding energies at 781.9 and 796.8 eV) and Co^{3+} (binding energies at 779.9 and 795.0 eV) and two shake-up satellites (binding energies at around 787.9 and 803.7 eV, identified as ‘‘Sat.’’). The high-resolution C 1s spectrum (Fig. 2(d)) consisted of three carbon peaks, which represent C–C/C=C (284.7 eV), C–O (285.8 eV), and C=O (288.7 eV) [26]. As shown in Fig. 2(c), the O 1s spectrum showed three peaks located at 529.5, 531.2, and 532.8 eV, which could be ascribed to the metal–oxygen bonds (O1, pink area), defects in oxygen (O2, blue area), and absorbed water (O3, green area) on the surface, respectively [27,28]. The defects in oxygen are due to the low oxygen coordination bond caused by the imbalance of cobalt ions and nickel ions between octahedral sites and tetrahedral sites. The existence of abundant defects in oxygen may result in the uneven distribution of local charges, thereby inducing dipole polarization under the electromagnetic field [29]. The oxygen defect ratio is expressed by the peak area ratio, and is shown in the inset of Fig. 2(c). Overall, the highly consistent characterization results of XRD, XPS, and Raman spectra collectively confirm the successful synthesis of $NiCo_2O_4$@CW composite.

Figure S3 in the ESM presents the room temperature hysteresis loops of $NiCo_2O_4$@CW (inset: enlarged view at low fields). The magnetization curve performs a typical ferromagnetic behavior, and the magnetization has been found to not saturate, even at the maximum applied field (10 kOe). The remnant magnetization and

coercivity were represented as 0.16 emu·g^{-1} and 62.5 Oe, respectively. It should be noted that low saturation magnetization implies the poor magnetic loss capacity.

SEM images of CW and $NiCo_2O_4$@CW are displayed in Fig. 3. Vertical direction of CW (Fig. 3(a)) and horizontal direction of CW (Fig. 3(b)) show that the CW has through, directional, and ordered channels, and the shape of the channels presents an irregular ellipse with a pore size of 10–30 μm and channel wall thickness of 1–3 μm. Vertical direction of $NiCo_2O_4$@CW (Fig. 3(c)) and horizontal direction of $NiCo_2O_4$@CW (Fig. 3(d)) demonstrate that the high-density short cone-like $NiCo_2O_4$ composites uniformly distributed in the through channels in CW. The thickness of carbon channel walls is obviously thinner than that of CW, because a large number of carbon atoms are dispersed in the $NiCo_2O_4$ hybrid in the heat treatment process, which can be further confirmed by energy dispersive X-ray spectroscopy (EDS) mapping images (Fig. S4 in the ESM). An image in the inset of Fig. 3(c) reveals the magnified cone-like $NiCo_2O_4$/C. The original size of the as-prepared samples was shown by optical photograph in Fig. S5 in the ESM. Simultaneously, the through, directional, and ordered channels were retained in the $NiCo_2O_4$@CW, and this unique ordered pore microstructure can enable abundant multiple reflections of electromagnetic waves and interfacial polarization, which are favorable for the MA performance.

Generally, the hybrid magnetic/dielectric composites present excellent EMW absorption capabilities due to electromagnetic complementation and impedance matching effects. Our ordered-channel $NiCo_2O_4$@CW composites with unique microstructure perform excellent MA abilities. Impedance matching ratio ($|Z_{in}/Z_0|$) is also an important parameter for EMW absorption. The impedance characteristic of the absorber is close to that of free space (the value of $|Z_{in}/Z_0|$ lose to 1), which means that the incident EMW can enter the absorber to the greatest extent [18]. Figure S6 in the ESM presents the RL curves and the impedance matching ratio of V-CW, H-CW, and V-$NiCo_2O_4$@CW samples with thickness from 1.0 to 5.5 mm in the frequency range of 2.0–18.0 GHz. It is observed that these three samples showed almost no MA (Figs. S6(a)–S6(c) in the ESM), resulting from poor impedance matching performance. Nevertheless, as shown in Figs. S6(d)–S6(f) in the ESM, the impedance matching performance of the three samples is found to be quite different. The impedance matching ratio of H-CW and V-$NiCo_2O_4$@CW are closer to 1 than that of V-CW, which implies that the through channels arranged horizontally relative to the incident direction of EMWs have better impedance matching performance than those arranged vertically, and are more conducive to EMWs loss, and the $NiCo_2O_4$ introduced in through channels also achieved the same effect. The RL value, impedance matching ratio, and EM parameters of disordered CW and $NiCo_2O_4$@CW samples demonstrated

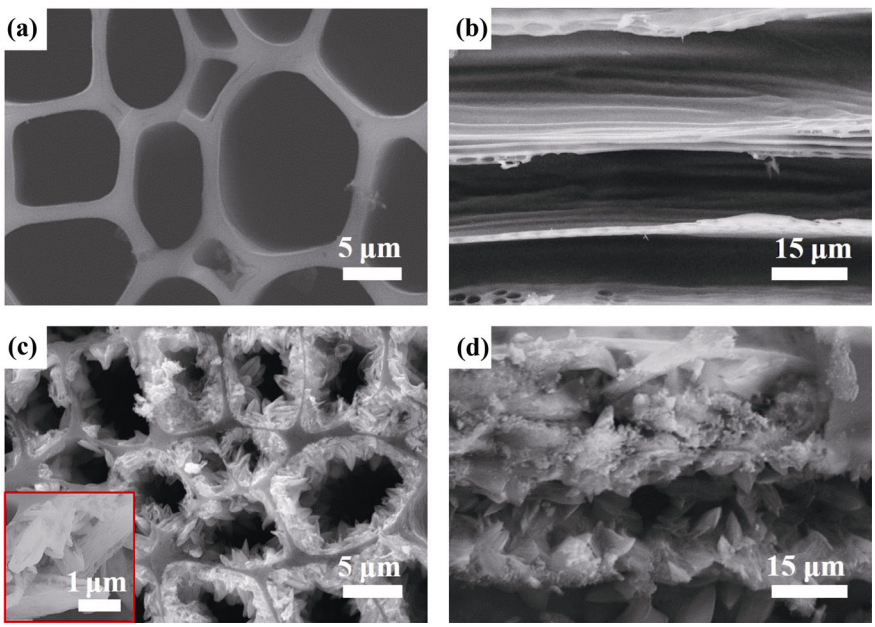

Fig. 3 SEM images of (a) V-CW, (b) H-CW, (c) V-$NiCo_2O_4$@CW, and (d) H-$NiCo_2O_4$@CW.

similar laws (Figs. S7 and S8 in the ESM). The sample of H-$NiCo_2O_4$@CW composites exhibited excellent EMW absorption capabilities with the $NiCo_2O_4$ distributed in through-channel arrangement horizontally. As observed from Fig. 4(c), the sample of H-$NiCo_2O_4$@CW reaches a strong absorption intensity of −64.02 dB at 10.72 GHz with the thickness of 3.62 mm, and the corresponding EAB value is 6.08 GHz (8.48–14.56 GHz). In particular, the maximum EAB value for the sample is 8.08 GHz (9.92–18.0 GHz) at the thickness of 3.2 mm, the super-wide EAB value could cover the entire Ku-band and the most X-band. We compare the performance of the H-$NiCo_2O_4$@CW sample to some similar materials reported in previous reports, the result is shown in Table 1. The excellent performance of RL, EAB, and thickness value clearly demonstrates the natural wood- derived carbon has great potential for MA. Unsurprisingly, the H-$NiCo_2O_4$@CW exhibits superior impedance matching at 2–5.5 mm thicknesses range with $|Z_{in}/Z_0|$ values between 0.75 and 1.25 in the 5–18 GHz range (Fig. 4(a)). Moreover, it is obvious that the RL peaks move to the lower frequency region as the thickness increased. This result can be explained by quarter-wavelength attenuation law, which means that when the absorber reaches the matching thickness (t_m), the reflected waves derived from the upper and bottom interface are out of phase by 180° and completely cancel each other in the air-absorber interface [30]:

$$t_m = \frac{n}{4}\lambda = \frac{nc}{4f\sqrt{|\mu_r\varepsilon_r|}} \quad (n = 1,3,5,\ldots) \tag{3}$$

where t_m is the matching thickness and λ, f, and c represent the wavelength, frequency, and velocity of the microwave, respectively. Obviously, the t_m values of the H-$NiCo_2O_4$@CW are basically consistent with the curve of quarter-wavelength attenuation model. What's more, by comparing the values of the $|Z_{in}/Z_0|$ and RL curve, the close correlation between them can clearly be found, that is, the closer the value of $|Z_{in}/Z_0|$ is to 1, the greater the RL value.

Generally speaking, the MA properties are not only controlled by impedance matching characteristics, but also affected by the attenuation energy capacity. Attenuation capacity is explained by that EMW is converted into other forms of energy inside absorber

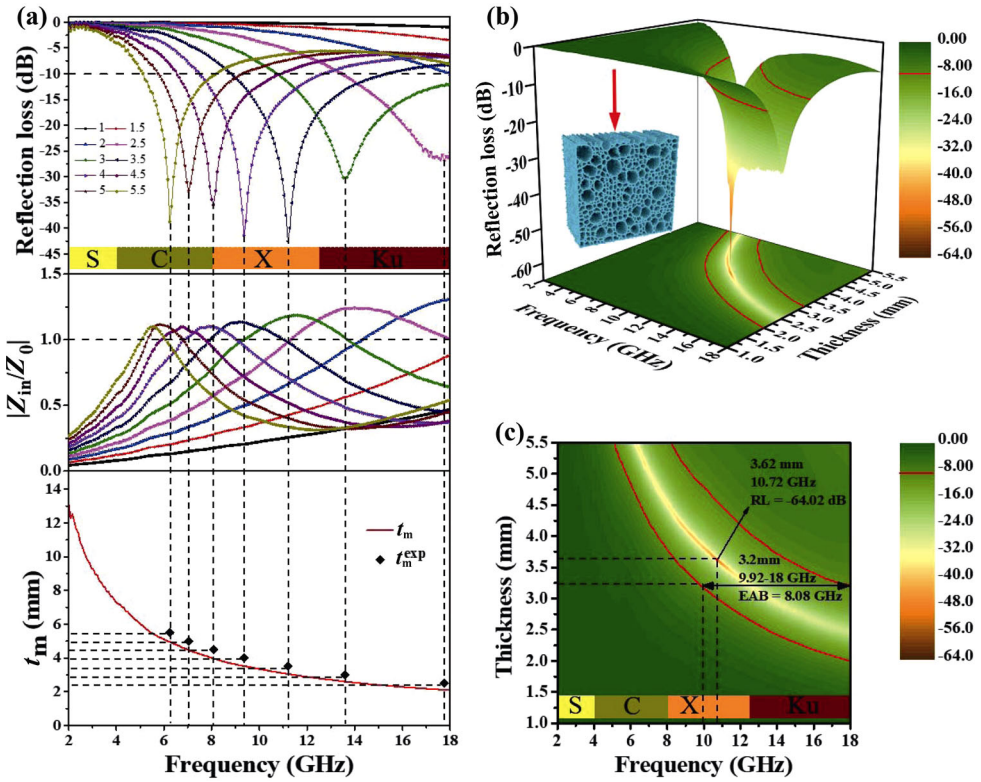

Fig. 4 (a) RL value, impedance matching ratio, actual thickness t_m^{exp}, and calculated thickness t_m for H-$NiCo_2O_4$@CW; (b) 3D RL value and (c) contour map of H-$NiCo_2O_4$@CW.

Table 1 MA performance of some porous carbon-based materials

Sample	Filling ratio (wt%)	RL_{min} (dB)/thickness (mm)	EAB_{max} (GHz)	Reference
PBPC[a]	—	−68.3/4.28	7.63	[15]
$NiCo_2S_4$/C	50	–64.7/1.91	5.26	[12]
FeCo/C@WC[b]	85	–47.6/1.5	8.9	[31]
CoFe/BPC[c]	—	–53.6/2.2	2.7	[32]
Fe_3N alloy/carbon	40	–65.6/2.05	6.76	[33]
Shaddock peel-based aerogel	20	–29.50/1.7	5.80	[34]
Co–$CoFe_2O_4$@PCHMs[d]	12.5	–65.31/2.1	8.48	[35]
Ni/NiO@C	20	–51.1/2.4	5.12	[36]
H-$NiCo_2O_4$@CW	26	–64.0/3.62	8.08	This work

[a]PBPC: porous biomass-pyrolyzed carbon.
[b]WC: wood carbon aerogel.
[c]BPC: biomass porous carbon.
[d]PCHMs: mesoporous hollow carbon spheres.

due to the existence of various loss mechanisms, such as conductivity loss, polarization loss, natural resonance, or eddy current loss, calculated as the attenuation constant (α) [37]:

$$\alpha=\frac{\sqrt{2}\pi f}{c}\sqrt{(\mu''\varepsilon''-\mu'\varepsilon')+\sqrt{(\mu''\varepsilon''-\mu'\varepsilon')^2+(\mu'\varepsilon''+\mu''\varepsilon')^2}} \quad (4)$$

From Fig. 5(a), it can be observed that the H-$NiCo_2O_4$@CW sample shows the largest α values, almost above 100 in the 2–18 GHz frequency range, indicating the stronger microwave attenuation ability of the H-$NiCo_2O_4$@CW sample than that of the other three samples, resulting in the $NiCo_2O_4$ distributed in through channels arranged horizontally. In addition, as a whole, the introduction of $NiCo_2O_4$ promoted the increase in attenuation capacity.

In order to explain the MA mechanisms of as-prepared materials, the complex permittivity (ε', ε''), permeability (μ', μ''), dielectric tangent loss ($\tan\delta_e=\varepsilon''/\varepsilon'$), and magnetic tangent loss ($\tan\delta_m=\mu''/\mu'$) are shown in Fig. 6. The real parts (ε' and μ') represent the stored capability of electric and magnetic energy while the imaginary parts (ε'' and μ'') represent the dissipated capability of electric and magnetic energy. $\tan\delta_e$ and $\tan\delta_m$ represent dielectric and magnetic loss capacities of the absorber, respectively [38]. From Figs. 6(a) and 6(b), it is observed that the ε' and ε'' values of the H-$NiCo_2O_4$@CW are larger than that of the other three samples, and possess a decreased trend as the frequency increases, which is attributed to the increased polarization hysteresis versus the higher frequency electric-field variation [39]. As for V-$NiCo_2O_4$@CW sample, its ε' and ε'' values are slightly higher than that of V-CW and H-CW, and basically do not change with the increase of frequency, showing a horizontal line relative to the frequency. The ε' values of V-CW and H-CW are the lowest, stay near 2, and do not change with frequency, and the ε'' values behave the same trend as ε'. The calculated $\tan\delta_e$ of all samples are depicted in Fig. 6(c). The curve of $\tan\delta_e$ value for the H-$NiCo_2O_4$@CW sample shows a trend of small fluctuations between 0.4 and 0.6, and the values are clearly higher than the other samples. As for other three samples, the trend of $\tan\delta_e$ value is similar to that of ε'' results, shown in Fig. 6(b). The H-$NiCo_2O_4$@CW sample presents the largest $\tan\delta_e$ value in 2–18 GHz frequency range compared with the other samples, demonstrating the best dielectric loss performance.

Generally speaking, the dielectric loss is closely associated with conductive loss and polarization loss, and the conductive loss lies on the electrical conductivity [40]. The introduction of $NiCo_2O_4$ could effectively enhance the conductive loss resulted from the high electrical conductivity. In detail, the $NiCo_2O_4$ hybrid uniformly distributed in the through channels formed by amorphous carbon, which allows the $NiCo_2O_4$@CW composites to form an efficient conductive network; this deduction could be confirmed by the ε'' curves of as-prepared samples, and the ε'' values of $NiCo_2O_4$@CW composites are larger than that of single CW. Simultaneously, the H-$NiCo_2O_4$@CW sample displays the strongest conductive loss capacity, and the conductivity of all samples shown in Fig. S9 in the ESM could prove the above points. The polarization

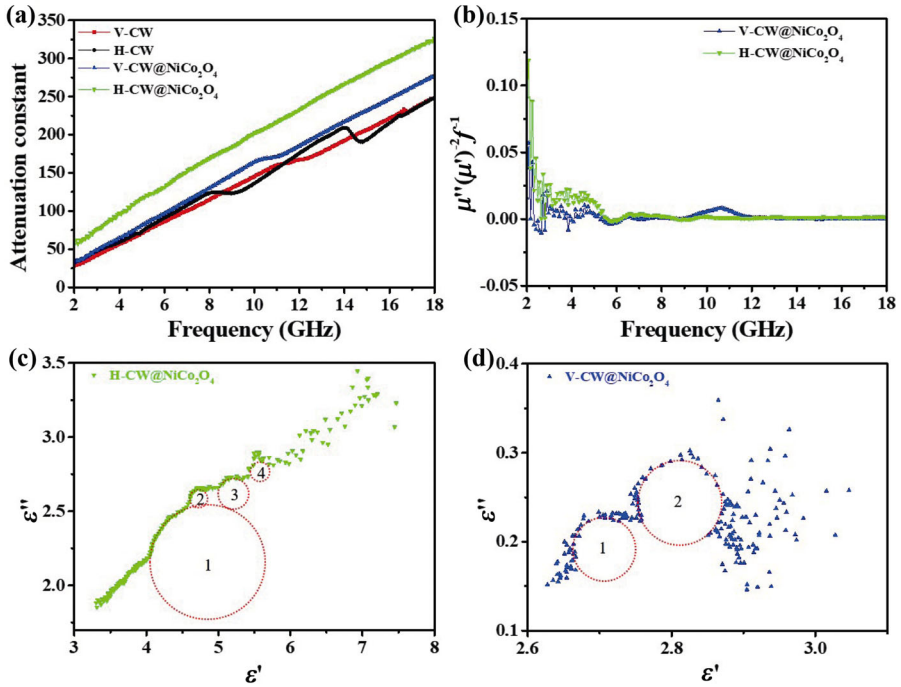

Fig. 5 (a) Attenuation constant α of all samples, (b) C_0 values versus frequency of V-$NiCo_2O_4$@CW and H-$NiCo_2O_4$@CW, and Cole–Cole curves of (c) H–$NiCo_2O_4$@CW and (d) V-$NiCo_2O_4$@CW.

loss comes from atomic polarization, electron polarization, dipole polarization, and interfacial polarization [41]. The atomic polarization and electron polarization could be eliminated firstly, because these two polarizations could only appear at higher frequency range. The dielectric loss for as-prepared samples should be mostly ascribed to the dipole polarization, which can be explained by the Cole–Cole model [42–44]:

$$\varepsilon_r = \varepsilon' - j\varepsilon'' = \varepsilon_\infty + \frac{\varepsilon_s - \varepsilon_\infty}{1 + j2\pi f\tau} \tag{5}$$

where ε_s, ε_∞, f, and τ stand for the static dielectric constant, the dielectric constant at infinite frequency, the frequency relaxation time, and the polarization relaxation time, respectively. And then the ε' and ε'' can be expressed as

$$\varepsilon' = \varepsilon_\infty + \frac{\varepsilon_s - \varepsilon_\infty}{1 + (2\pi f)^2\tau^2} \tag{6}$$

$$\varepsilon'' = \frac{2\pi f\tau(\varepsilon_s - \varepsilon_\infty)}{1 + (2\pi f)^2\tau^2} \tag{7}$$

Consequently, the relationship between ε' and ε'' can be depicted as

$$\left(\varepsilon' - \frac{\varepsilon_s + \varepsilon_\infty}{2}\right)^2 + (\varepsilon'')^2 = \left(\frac{\varepsilon_s - \varepsilon_\infty}{2}\right)^2 \tag{8}$$

Therefore, the relationship between ε' and ε'' can be determined as a single semicircle, called the Cole–Cole semicircle, and each Cole–Cole semicircle represents a Debye dipolar relaxation process. Figures 5(c), 5(d), and Fig. S10 in the ESM demonstrate the Cole–Cole curves of all tested samples in the 2–18 GHz frequency range. As mentioned above, enhancement of the Debye dipolar relaxation is definitely reflected in the increasing number of semicircles [45,46]. As for V-CW and H-CW (Fig. S10 in the ESM), the points on the curves are concentrated in a small range, which will lead to the existence of a large number of Cole–Cole semicircles. It can be inferred that the numerous defects within the CW were served as the polarization centers to promote the formation of Debye dipole polarization, which could be confirmed by the result of I_D/I_G value in Fig. 2(b). However, the strongest Debye relaxation of CW results in extremely poor conductivity and eventually leads to improper impedance matching. The existence of $NiCo_2O_4$ not only reduces the I_D/I_G value of CW (Fig. 2(b)) to improve conductivity and impedance matching, but also causes interfacial polarization to increase the dielectric loss capability. The number of Cole–Cole semicircles is reduced to a level that can be basically identified in the Cole–Cole curves of H-$NiCo_2O_4$@CW and V-$NiCo_2O_4$@CW samples, which implies the dielectric

loss for $NiCo_2O_4$@CW hybrid composites should not mainly come from the Debye dipolar relaxation, and the conductive loss and interfacial polarization should play a dominant role in dielectric loss.

Figures 6(d) and 6(e) present the changes of complex permeability in the frequency range of 2–18 GHz for the H-$NiCo_2O_4$@CW and V-$NiCo_2O_4$@CW samples. The μ' and μ'' slightly fluctuated with frequency, and varied in the range of 0.90–1.05 and 0–0.17, respectively. Meanwhile, the values of the calculated magnetic loss tangent $\tan\delta_m$ of these two samples were depicted in Fig. 6(f), the values are almost below 0.2, and there is no obvious resonance peak appearing on the curves, which means that the magnetic loss does not contribute much to the MA performance. In general, magnetic loss mainly results from natural resonance, exchange resonance, and eddy current loss in the microwave frequency bands [47].

Here, the low-frequency resonance is mainly assigned to the natural resonance, while the exchange resonance almost takes place at higher frequencies [48]. The eddy current loss effect could be demonstrated by the C_0 curve [49]:

$$C_0 = \frac{\mu''}{(\mu')^2 f} \tag{9}$$

If the eddy current loss is the dominated factor for the magnetic loss, the value of C_0 should be a constant, which makes the C_0 value appear as a horizontal line in C_0–f curve. As shown in Fig. 5(b), in 2–7 GHz

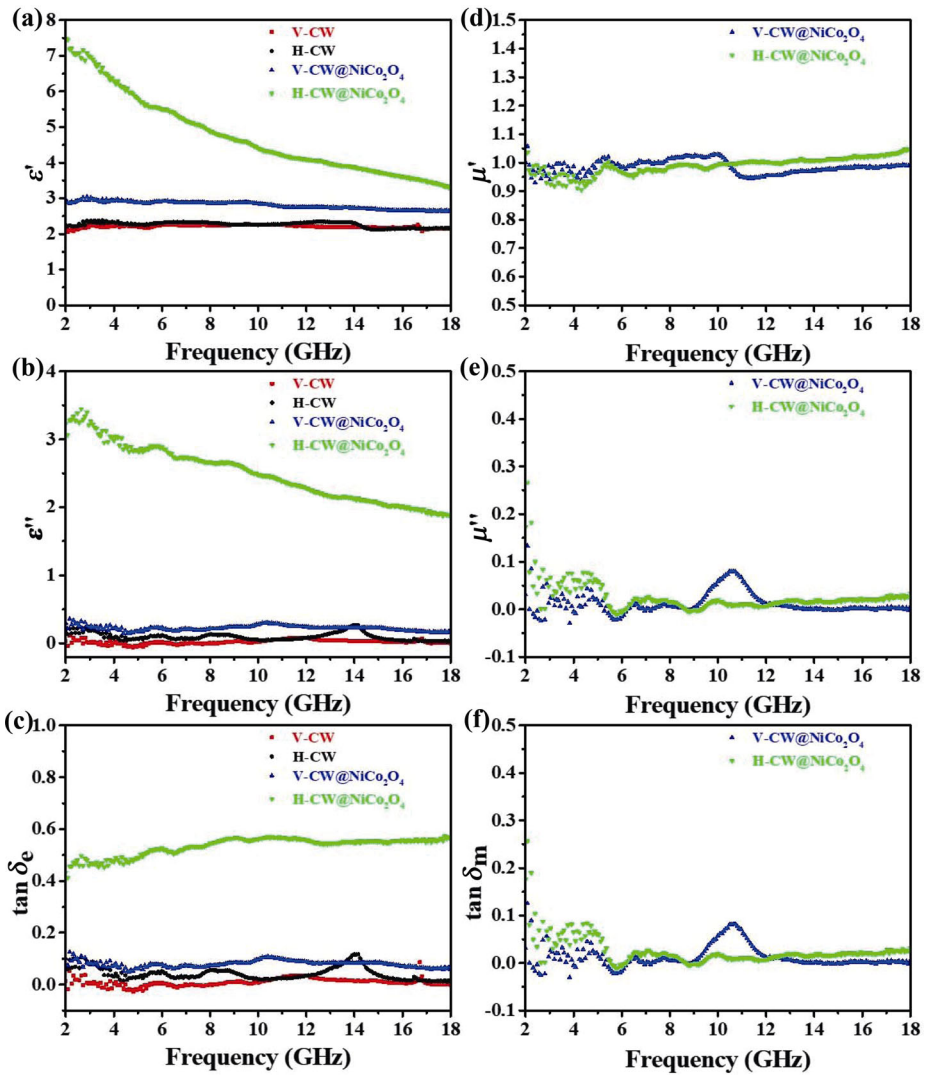

Fig. 6 EM parameters of samples: (a) real part ε' and (b) imaginary part ε'' of permittivity, (c) dielectric loss $\tan\delta_e$, (d) real part μ' and (e) imaginary part μ'' of permeability, and (f) magnetic loss $\tan\delta_m$.

frequency range, the noticeable resonance peaks can be detected, which is assigned to natural resonance. The C_0 curve of H-$NiCo_2O_4$@CW nearly never changed in the frequency range of 7–18 GHz, while a tiny resonance peak was found in the C_0 curve of V-$NiCo_2O_4$@CW at 10.5 GHz. The huge difference of MA performance between H-$NiCo_2O_4$@CW and V-$NiCo_2O_4$@CW samples is discovered in Fig. 4 and Fig. S6(c) in the ESM, while the magnetic parameters of them behave basically similar, which implies that the dielectric loss controlled by microstructure and composition is the main influence factor on absorbing EMW.

In order to explore the influence of the arrangement direction of ordered channels on the performance of MA, the two channel arrangement directions of $NiCo_2O_4$@CW composite were constructed as simplified models for finite element analysis (FEA) simulation. The simplified model of V-$NiCo_2O_4$@CW is demonstrated in Fig. 7, with the channel diameter and channel wall thickness set to 10 and 3 μm, respectively, which is derived from the SEM pictures of actual structure shown in Figs. 3(c) and 3(d). In addition, the inside of the channels is filled with paraffin wax, and the section to be explored is marked in the model diagram. The frequency parameter of the simulation calculation process was set to 10.72 GHz. The time-average power flow (*poav*) of section 1 and section 2 are shown in Figs. 7(b) and 7(c). The *poav* can be regarded as the propagation path and energy distribution of EMW inside the material, which is reflected in the direction and size of *poav* arrow. Obviously, the vertical channel is less obstructive to the EMW, and the EMW can easily pass through the channel without sufficient interaction with the material. Furthermore, Figs. 7(d)–7(f) prove that V-$NiCo_2O_4$@CW composite has little attenuation ability to EMW. As for H-$NiCo_2O_4$@CW, the transmission direction and intensity of EMW change significantly near the channel walls (Fig. 8(b)), which indicates that the material has an effective interaction with microwave, due to multiple reflection and scattering caused by ordered porous structure. Simultaneously, as shown in Figs. 8(c)–8(e), strong dielectric loss occurs near the channel walls, resulted from the high-efficiency conductive network formed by CW decorated with $NiCo_2O_4$ hybrids and polarization relaxation. It is worth noting that the intensity distributions of total loss power density (Fig. 8(c)) and dielectric loss power density (Fig. 8(d)) are very similar and the intensity of magnetic loss power density (Fig. 8(e)) is extremely low compared to dielectric loss power density. In other words, the contribution of magnetic loss to MA is extremely small compared to dielectric loss, and this result is consistent with the previous analysis of EM parameters.

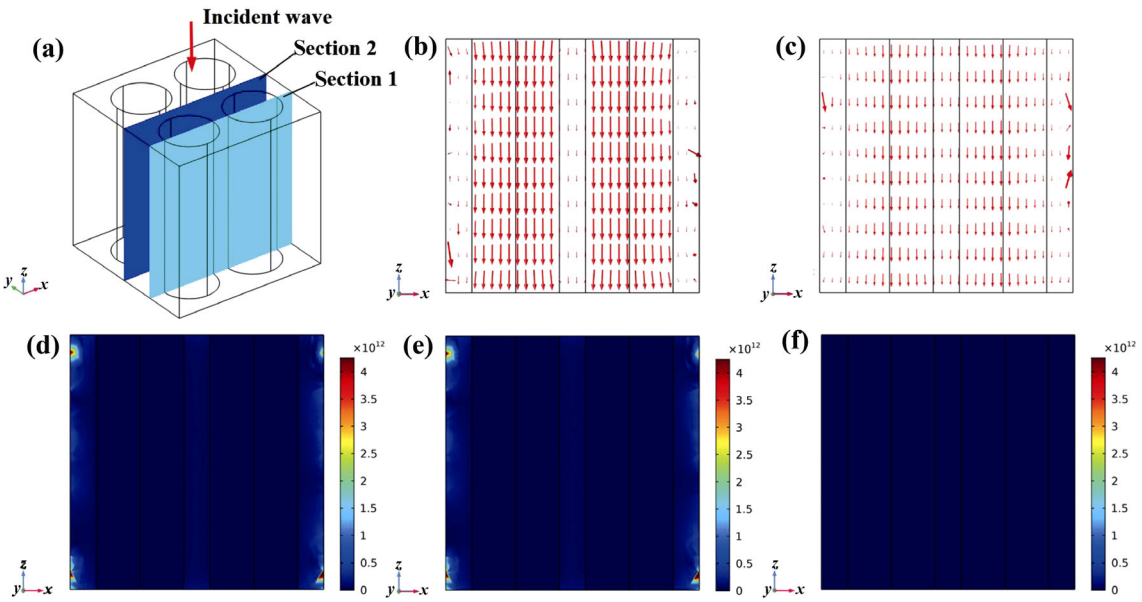

Fig. 7 FEA simulation of V-$NiCo_2O_4$@CW. (a) Schematic diagram of simplified model and section position, (b) time-average power flow *poav* ($W \cdot m^{-2}$), (c) time-average power flow *poav* ($W \cdot m^{-2}$) in section 2, (d) total loss power density Q ($W \cdot m^{-3}$), (e) dielectric loss power density Q_e ($W \cdot m^{-3}$), and (f) magnetic loss power density Q_m ($W \cdot m^{-3}$) in section 1.

In summary, the possible MA mechanism of the H-$NiCo_2O_4$@CW hybrid composites is described in Fig. 9. Firstly, the $NiCo_2O_4$ hybrids infiltrated into a large number of carbon atoms are uniformly distributed

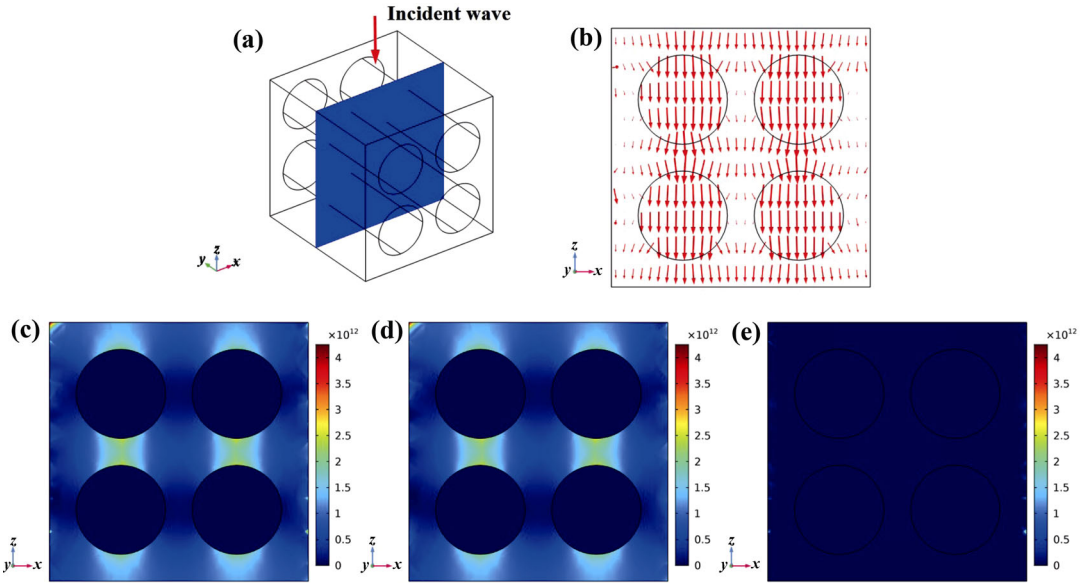

Fig. 8 FEA simulation of H-$NiCo_2O_4$@CW. (a) Schematic diagram of simplified model and section position, (b) time-average power flow *poav* ($W \cdot m^{-2}$), (c) total loss power density Q ($W \cdot m^{-3}$), (d) dielectric loss power density Q_e ($W \cdot m^{-3}$), and (e) magnetic loss power density Q_m ($W \cdot m^{-3}$) in section 1.

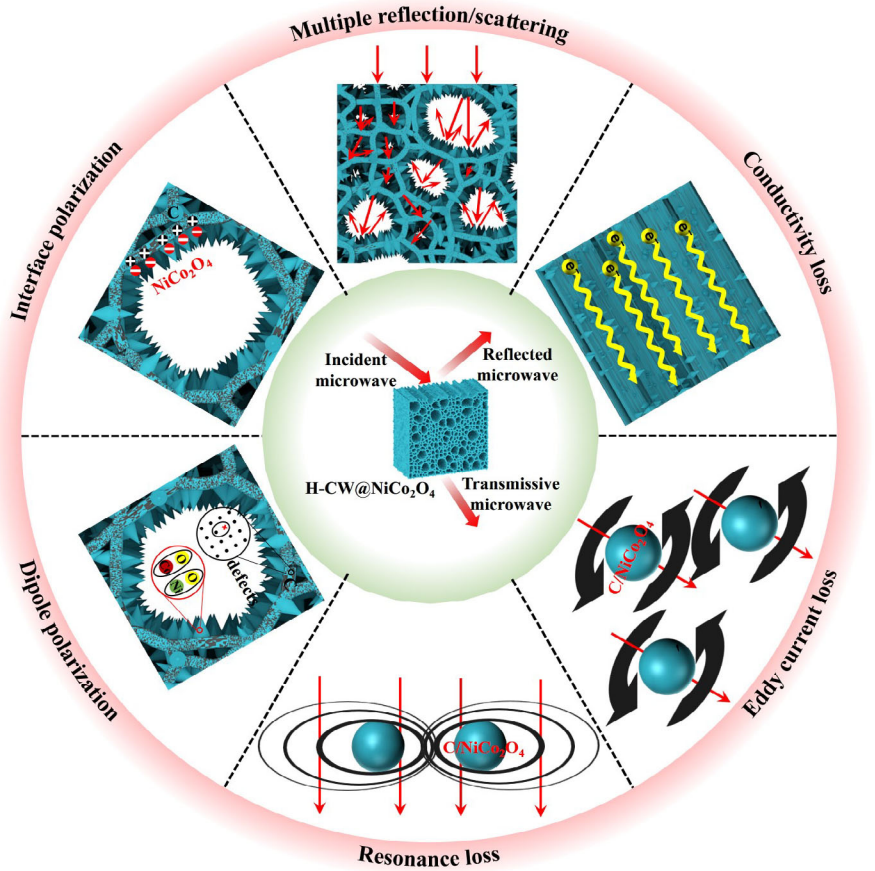

Fig. 9 Schematic illustration for the EMW absorption of H-$NiCo_2O_4$@CW.

on the wall of the ordered channels, resulting in that the conductivity of the material is effectively enhanced, so that the 3D conductive skeleton derived from natural wood would promote the electron transportation and improve the dielectric loss ability. Secondly, the interface between carbon and $NiCo_2O_4$ would form non-uniform charge distribution and interfacial polarization loss because of the difference of electrical conductivity. Thirdly, the presence of defects within the amorphous carbon and $NiCo_2O_4$ hybrids would serve as the polarization centers to induce the multiple reflection and scattering processes. Fourthly, the magnetic loss including natural resonance and eddy current loss should also contribute to the MA property to a slight extent. Therefore, benefiting from the matched impedance and the enhanced attenuation constant, the CW with horizontally ordered channels decorated by cone-like $NiCo_2O_4$ hybrids (H-$NiCo_2O_4$@CW) exhibit the outstanding MA performance.

4 Conclusions

This work reported a wood-derived carbon-based material with ordered channels decorated by $NiCo_2O_4$ hybrids, which is manufactured through a facile, low-cost, and sustainable method with outstanding EMW absorption performance. The combination of 3D carbon skeleton with horizontal ordered channels derived from natural wood and $NiCo_2O_4$ hybrids together enable multiple EMW loss mechanisms to be effectively realized, resulting in the matched impedance and the enhanced attenuation constant. The horizontal arrangement of the through channels of $NiCo_2O_4$@CW (H-$NiCo_2O_4$@CW) exhibits a strong reflection loss value of −64.0 dB at 10.72 GHz with a thickness of 3.62 mm and a low filling ratio of 26%, and the EAB is 8.08 GHz (9.92–18.0 GHz) at the thickness of 3.2 mm. The result of FEA simulation confirms that the horizontal arrangement of ordered channels allows the material to interact effectively with EMW, thereby obtaining excellent MA property. This research provides a facile and novel strategy for using CW to fabricate advanced microwave absorbers with light weight and strong attenuation capabilities.

Acknowledgements

This work was supported by the National Natural Science Foundation of China (NSFC, Grant Nos. 51772060, 51372052, and 51621091).

Electronic Supplementary Material

Supplementary material is available in the online version of this article at https://doi.org/10.1007/s40145-021-0520-z.

References

[1] Wang FY, Wang N, Han XJ, *et al*. Core–shell FeCo@carbon nanoparticles encapsulated in polydopamine-derived carbon nanocages for efficient microwave absorption. *Carbon* 2019, **145**: 701–711.

[2] Yan J, Huang Y, Chen C, *et al*. The 3D CoNi alloy particles embedded in N-doped porous carbon foams for high-performance microwave absorbers. *Carbon* 2019, **152**: 545–555.

[3] Pang YQ, Li YF, Wang JF, *et al*. Carbon fiber assisted glass fabric composite materials for broadband radar cross section reduction. *Compos Sci Technol* 2018, **158**: 19–25.

[4] Arjmand M, Chizari K, Krause B, *et al*. Effect of synthesis catalyst on structure of nitrogen-doped carbon nanotubes and electrical conductivity and electromagnetic interference shielding of their polymeric nanocomposites. *Carbon* 2016, **98**: 358–372.

[5] Li F, Zhan WW, Su YT, *et al*. Achieving excellent electromagnetic wave absorption of $ZnFe_2O_4$@CNT/polyvinylidene fluoride flexible composite membranes by adjusting processing conditions. *Compos A*: *Appl Sci Manuf* 2020, **133**: 105866.

[6] Quan B, Gu WH, Sheng JQ, *et al*. From intrinsic dielectric loss to geometry patterns: Dual-principles strategy for ultrabroad band microwave absorption. *Nano Res* 2021, **14**: 1495–1501.

[7] Hou TQ, Jia ZR, Wang BB, *et al*. Metal-organic framework-derived $NiSe_2$–$CoSe_2$@C/$Ti_3C_2T_x$ composites as electromagnetic wave absorbers. *Chem Eng J* 2021, **422**: 130079.

[8] Shi YN, Gao XH, Qiu J. Synthesis and strengthened microwave absorption properties of three-dimensional porous Fe_3O_4/graphene composite foam. *Ceram Int* 2019, **45**: 3126–3132.

[9] Xiong CY, Li BB, Liu HG, *et al*. A smart porous wood-supported flower-like NiS/Ni conjunction with vitrimer co-effect as a multifunctional material with reshaping, shape-memory, and self-healing properties for applications in high-performance supercapacitors, catalysts, and sensors. *J Mater Chem A* 2020, **8**: 10898–10908.

[10] Zhang WY, Yang YN, Xia RQ, *et al*. Graphene-quantum-dots-induced MnO_2 with needle-like nanostructure grown on carbonized wood as advanced electrode for supercapacitors. *Carbon* 2020, **162**: 114–123.

[11] Chen BL, Gsalla A, Gaur A, *et al*. Porous wood monoliths decorated with platinum nano-urchins as catalysts for underwater micro-vehicle propulsion via H_2O_2 decomposition. *ACS Appl Nano Mater* 2019, **2**: 4143–4149.

[12] Dong S, Hu PT, Li XT, *et al*. $NiCo_2S_4$ nanosheets on 3D wood-derived carbon for microwave absorption. *Chem Eng J* 2020, **398**: 125588.

[13] Zheng Y, Song YJ, Gao T, *et al*. Lightweight and hydrophobic three-dimensional wood-derived anisotropic magnetic porous carbon for highly efficient electromagnetic interference shielding. *ACS Appl Mater Interfaces* 2020, **12**: 40802–40814.

[14] Wei S, Wang XX, Zhang BQ, *et al*. Preparation of hierarchical core–shell C@$NiCo_2O_4$@Fe_3O_4 composites for enhanced microwave absorption performance. *Chem Eng J* 2017, **314**: 477–487.

[15] Xi JB, Zhou EZ, Liu YJ, *et al*. Wood-based straightway channel structure for high performance microwave absorption. *Carbon* 2017, **124**: 492–498.

[16] Dhavale SB, Patil VL, Beknalkar SA, *et al*. Study of solvent variation on controlled synthesis of different nanostructured $NiCo_2O_4$ thin films for supercapacitive application. *J Colloid Interface Sci* 2021, **588**: 589–601.

[17] Jang KB, Park KR, Kim KM, *et al*. Electrochemical performance of the spinel $NiCo_2O_4$ based nanostructure synthesized by chemical bath method for glucose detection. *Appl Surf Sci* 2021, **545**: 148927.

[18] Liu XF, Hao CC, Jiang H, *et al*. Hierarchical $NiCo_2O_4$/Co_3O_4/NiO porous composite: A lightweight electromagnetic wave absorber with tunable absorbing performance. *J Mater Chem C* 2017, **5**: 3770–3778.

[19] Zhao HB, Cheng JB, Zhu JY, *et al*. Ultralight CoNi/rGO aerogels toward excellent microwave absorption at ultrathin thickness. *J Mater Chem C* 2019, **7**: 441–448.

[20] Yan X, Huang XX, Chen YT, *et al*. A theoretical strategy of pure carbon materials for lightweight and excellent absorption performance. *Carbon* 2021, **174**: 662–672.

[21] Xu W, Wang GS, Yin PG. Designed fabrication of reduced graphene oxides/Ni hybrids for effective electromagnetic absorption and shielding. *Carbon* 2018, **139**: 759–767.

[22] Wang L, Yu XF, Li X, *et al*. Conductive-network enhanced microwave absorption performance from carbon coated defect-rich Fe_2O_3 anchored on multi-wall carbon nanotubes. *Carbon* 2019, **155**: 298–308.

[23] Wang X, Pan F, Xiang Z, *et al*. Magnetic vortex core–shell Fe_3O_4@C nanorings with enhanced microwave absorption performance. *Carbon* 2020, **157**: 130–139.

[24] Wu HJ, Wu GL, Ren YY, *et al*. Co^{2+}/Co^{3+}ratio dependence of electromagnetic wave absorption in hierarchical $NiCo_2O_4$–$CoNiO_2$ hybrids. *J Mater Chem C* 2015, **3**: 7677–7690.

[25] Qin M, Zhang LM, Wu HJ. Dual-template hydrothermal synthesis of multi-channel porous $NiCo_2O_4$ hollow spheres as high-performance electromagnetic wave absorber. *Appl Surf Sci* 2020, **515**: 146132.

[26] Qin ZH, Wang CY, Wang JJ, *et al*. Spherical shape Co@Co_3O_4 core–shell composites grown on surface of graphite nanosheets with ultra-thin and excellent electromagnetic absorption performance. *Appl Surf Sci* 2021, **539**: 148253.

[27] Xu X, Ran F, Fan Z, *et al*. Bimetallic metal-organic framework-derived pomegranate-like nanoclusters coupled with CoNi-doped graphene for strong wideband microwave absorption. *ACS Appl Mater Interfaces* 2020, **12**: 17870–17880.

[28] Qin M, Zhang LM, Zhao XR, *et al*. Defect induced polarization loss in multi-shelled spinel hollow spheres for electromagnetic wave absorption application. *Adv Sci* 2021, **8**: 2004640.

[29] Chang Q, Liang HS, Shi B, *et al*. Ethylenediamine-assisted hydrothermal synthesis of $NiCo_2O_4$ absorber with controlled morphology and excellent absorbing performance. *J Colloid Interface Sci* 2021, **588**: 336–345.

[30] Wu HJ, Zhao ZH, Wu GL. Facile synthesis of FeCo layered double oxide/raspberry-like carbon microspheres with hierarchical structure for electromagnetic wave absorption. *J Colloid Interface Sci* 2020, **566**: 21–32.

[31] Xiong Y, Xu LL, Yang CX, *et al*. Implanting FeCo/C nanocages with tunable electromagnetic parameters in anisotropic wood carbon aerogels for efficient microwave absorption. *J Mater Chem A* 2020, **8**: 18863–18871.

[32] Ji C, Liu Y, Li YY, *et al*. Facile preparation and excellent microwave absorption properties of cobalt–iron/porous carbon composite materials. *J Magn Magn Mater* 2021, **527**: 167776.

[33] Gu WH, Cui XQ, Zheng J, *et al*. Heterostructure design of Fe_3N alloy/porous carbon nanosheet composites for efficient microwave attenuation. *J Mater Sci Technol* 2021, **67**: 265–272.

[34] Gu WH, Sheng JQ, Huang QQ, *et al*. Environmentally friendly and multifunctional shaddock peel-based carbon aerogel for thermal-insulation and microwave absorption. *Nano-Micro Lett* 2021, **13**: 102.

[35] Zhang HX, Jia ZR, Wang BB, *et al*. Construction of remarkable electromagnetic wave absorber from heterogeneous structure of Co–$CoFe_2O_4$@mesoporous hollow carbon spheres. *Chem Eng J* 2021, **421**: 129960.

[36] Zhou XF, Jia ZR, Zhang XX, *et al*. Controllable synthesis of Ni/NiO@porous carbon hybrid composites towards remarkable electromagnetic wave absorption and wide absorption bandwidth. *J Mater Sci Technol* 2021, **87**: 120–132.

[37] Liu PB, Gao S, Wang Y, *et al*. Core–shell Ni@C encapsulated by N-doped carbon derived from nickel-organic polymer coordination composites with enhanced microwave absorption. *Carbon* 2020, **170**: 503–516.

[38] Wang Y, Di XC, Lu Z. Controllable construction design of Co@C@MWCNTs interpenetrating composite with tunable enhanced electromagnetic wave absorption. *J Mater Sci*: *Mater Electron* 2021, **32**: 1061–1072.

[39] Wang JW, Wang BB, Feng AL, *et al*. Design of morphology-controlled and excellent electromagnetic wave absorption performance of sheet-shaped $ZnCo_2O_4$ with a special arrangement. *J Alloys Compd* 2020, **834**: 155092.

[40] Dong S, Zhang WZ, Zhang XH, *et al*. Designable synthesis of core–shell SiCw@C heterostructures with thickness-dependent electromagnetic wave absorption between the whole X-band and Ku-band. *Chem Eng J* 2018, **354**: 767–776.

[41] Zhang HX, Jia ZR, Feng AL, *et al*. Enhanced microwave absorption performance of sulfur-doped hollow carbon microspheres with mesoporous shell as a broadband absorber. *Compos Commun* 2020, **19**: 42–50.

[42] Zhang MM, Jiang ZY, Si HX, *et al*. Heterogeneous iron–nickel compound/RGO composites with tunable microwave absorption frequency and ultralow filler loading. *Phys Chem Chem Phys* 2020, **22**: 8639–8646.

[43] Wang XY, Lu YK, Zhu T, *et al*. $CoFe_2O_4$/N-doped reduced graphene oxide aerogels for high-performance microwave absorption. *Chem Eng J* 2020, **388**: 124317.

[44] Yan X, Huang XX, Zhong B, *et al*. Balancing interface polarization strategy for enhancing electromagnetic wave absorption of carbon materials. *Chem Eng J* 2020, **391**: 123538.

[45] Chen JP, Jia H, Liu Z, *et al*. Construction of C–Si heterojunction interface in SiC whisker/reduced graphene oxide aerogels for improving microwave absorption. *Carbon* 2020, **164**: 59–68.

[46] Gao XR, Jia ZR, Wang BB, *et al*. Synthesis of NiCo–LDH/MXene hybrids with abundant heterojunction surfaces as a lightweight electromagnetic wave absorber. *Chem Eng J* 2021, **419**: 130019.

[47] Lyu N, Wang JH, Shen HJ, *et al*. Graphene quantum dots interfacial-decorated hierarchical Ni/PS core/shell nanocapsules for tunable microwave absorption. *J Alloys Compd* 2020, **848**: 156529.

[48] Zhang X, Qiao J, Zhao JB, *et al*. High-efficiency electromagnetic wave absorption of cobalt-decorated NH_2-UIO-66-derived porous ZrO_2/C. *ACS Appl Mater Interfaces* 2019, **11**: 35959–35968.

[49] Yu JY, Chi FL, Sun YP, *et al*. Assembled porous Fe_3O_4@g-C_3N_4 hybrid nanocomposites with multiple interface polarization for stable microwave absorption. *Ceram Int* 2018, **44**: 19207–19216.